DE GRUYTER Science and Engineering of Composite Materials 2023; 30: 20220200

Research Article

Lei Fan, Chun Hu, Neng Yang, Xingshuai Fan, Jie Cheng* and Xiangming Li

Gradient-distributed ZTAp-VCp/Fe45 as new anti-wear composite material and its bonding properties during composite casting

https://doi.org/10.1515/secm-2022-0200
received November 15, 2022; accepted April 16, 2023

Abstract: In this article, gradient-distributed VCp-ZTAp/Fe45 composites were prepared by vacuum sintering, and three-body abrasive wear experiments were carried out to investigate its anti-wear performance. The composite casting of VCp-ZTAp/Fe45 was investigated by using the finite element method and experiments, and the bonding between the Fe45 substrate and 35SiMnCrMoNi steel was fully investigated. Results show the *in situ* formation of VCp in the VCp-ZTAp/Fe45 composite matrix during vacuum sintering. The anti-wear property of the VCp-ZTAp/Fe45 composite is ca. 7 times that of Hardox450 and NM450 and ca. 8 times of 30SiMn. There forms a solid metallurgical bonding between the Fe45 matrix of VCp-ZTAp/Fe45 and 35SiMnCrMoNi steel, with a ca. 80 μm thickness of the bonding area during the composite casting.

Keywords: composite material, abrasive wear, finite element method

1 Introduction

Coal is the most widely used fossil energy at present, but the harsh working conditions of coal mining equipment make the key components (such as shearer pick seat and scraper conveyor) suffer from serious abrasion [1–4]. The resulting frequent maintenance and parts replacement caused huge economic losses. In order to improve the wear resistance of key components in coal mining equipment, it is necessary to develop new materials that have improved wear resistance. Particle-reinforced iron-based composites have received extensive attention from researchers due to high mechanical strength and good wear resistance [5–8]. The common reinforcing phase particles mainly include titanium carbide (TiC) [9,10], aluminum oxide (Al_2O_3) [11,12], vanadium carbide (VC) [13], tungsten carbide (WC) [14] and zirconia toughened alumina (ZTA) [15–18]. Dong et al. [9] prepared TiC-reinforced iron matrix composites and studied the anti-wear performance by the two-body abrasive wear tests. Results show that when the load is 1.5 kg, the relative wear resistance of TiC-reinforced iron matrix composites is 2.67 times that of pure gray cast iron. Li et al. [15] prepared ZTAp–Fe composites and found the ZTAp well combines with iron matrix and the ZTAp–Fe composite material has good compressive strength. Our previous research [19] proves the bonding properties of ZTAp with iron matrix could be improved by treating the surface of ZTAp with nickel plating. Research from Wang et al. [17] show the ZTAp–Fe composites have better impact wear resistance than pure iron matrix materials. Vanadium (V) is easy to react with carbon (C) to form VCp at high temperatures, and the ratio of V to C decreases with the increase of carbon element in the reaction process [20,21]. The VC content was also proved to affect the microstructure and the mechanical properties of VC/Fe matrix composites [22]. Besides, the influences of the sintering temperature on the densification of Fe–VC composites was also investigated during the *in-situ* synthesis process [23]. However, the research on particle-reinforced iron

---

* **Corresponding author: Jie Cheng,** School of Mechatronics and Information Engineering, China University of Mining and Technology-Beijing, Beijing, 100083, China; Key Laboratory of Intelligent Mining and Robotics, Ministry of Emergency Management, Beijing, 100083, China, e-mail: jiecheng@cumtb.edu.cn
Lei Fan: School of Mechatronics and Information Engineering, China University of Mining and Technology-Beijing, Beijing, 100083, China; Key Laboratory of Intelligent Mining and Robotics, Ministry of Emergency Management, Beijing, 100083, China; State Key Laboratory of Tribology in Advanced Equipment, Tsinghua University, Beijing, 100084, China
Chun Hu, Neng Yang, Xingshuai Fan: School of Mechatronics and Information Engineering, China University of Mining and Technology-Beijing, Beijing, 100083, China; Key Laboratory of Intelligent Mining and Robotics, Ministry of Emergency Management, Beijing, 100083, China
Xiangming Li: National-Local Joint Engineering Laboratory for Technology of Advanced Metallic Solidification Forming and Equipment, Faculty of Material Science and Engineering, Kunming University of Science and Technology, Kunming 650093, China

matrix composites mainly focuses on that using a single reinforcing phase particle. Few reports could be found on that using the mixed reinforcing phase particles or the wear-resistance of the composite materials.

Casting is an important process in the preparation of key components of large coal mining equipment. Therefore, it is of great importance to develop the casting technique in order to facilitate the application of particle-reinforced iron-based composite materials in industries. Tayal et al. [24] used composite casting technology to join pure Mg and Al alloy (A356) together and proved that the graph theory approach was an effective tool to evaluate the optimal parameters for the composite casting process. Bakke et al. [25] achieved a high-quality bond between cast Al alloy (A356) and pure Cu through a gravity composite casting. Tensile tests showed that the bimetallic interface obtains a maximum ultimate tensile strength of 90.8 MPa. Fan et al. [26] studied the pouring temperature on the microstructure of Mg/Al steel bimetallic castings prepared by the composite casting process, and results showed that the interfacial bonding is the most stable when the casting temperature is 780°C. The investigations on composite casting nowadays are generally done by experiments, and there is little work done by theoretical simulation combined with experiments, which is of great significance in revealing the formation mechanism of the interface transition zone after composite casting.

In this work, the vacuum sintering was used to prepare the VCp-ZTAp/Fe45 composite material, and the strengthening mechanism was investigated. In order to make the bond of the cladding metal and the VCp-ZTAp/Fe45 composite material more stable during composite casting, the VCp-ZTAp/Fe45 composite is gradient-distributed, with an upper layer of VCp-ZTAp/Fe45 and a lower layer of Fe45 matrix. The three-body abrasive wear experiment was carried out on the VCp-ZTAp/Fe45 composites to study their anti-wear property. Finite element method (FEM) was used to study the surface temperature change and internal temperature field distribution of the Fe45 matrix layer in composite casting. The interface between the VCp-ZTAp/Fe45 composites and the cladding material was analyzed microscopically. Combining the simulation and experimental methods, the bonding between the VCp-ZTAp/Fe45 and the cladding layer was revealed.

2 Experimental and simulation

This article describes the preparation of VCp-ZTAp/Fe45 composites and the characterization of the materials. The three-body abrasive wear performance of VCp-ZTAp/Fe45 composites was studied based on the key components of coal mine general mining equipment which are subjected to wear conditions during operation.

2.1 Preparation and characterization of VCp-ZTAp/Fe45 composites

Gradient VCp-ZTAp/Fe45 composites were prepared by vacuum sintering method. The metal matrix is Fe45 powder with an average particle size of 50 μm. The morphology of Fe45 powder and ZTAp is shown in Figure 1(a) and (b), respectively. The element content of ISA is shown in Table 1. The *in-situ* self-generation technology was used to introduce VCp as the second reinforcing phase. The ISA powder was added with ferrovanadium powder (element content shown in Table 1) and carbon black powder. The mass ratio of the mixed ferrovanadium powder to carbon black powder was 1:8.5. The mixed powder was added to the Fe45 powder at a mass fraction of 5%. Planetary ball milling machine was used to mix the powder. The milling

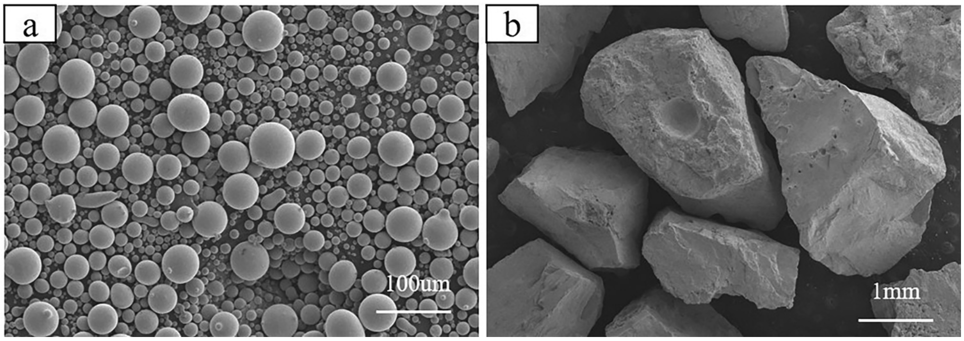

Figure 1: Raw material morphology: (a) Fe45 powder; (b) ZTA particle.

Table 1: Element content of Fe45, ferrovanadium, and 35SiMnCrMoNi powder

(wt%)	C	Si	Mn	Cr	Mo	Ni	Fe	B	V	Al
Fe45	0.098	0.57	—	15.5	—	0.065	79.2	1.33	—	—
Ferrovanadium	0.40	2.00	—	—	—	—	46.00	—	50.00	1.5
35SiMnCrMoNi	0.36	0.50	1.14	1.10	0.21	0.59	96.10	—	—	—

time was 1.5 h and the mass ratio of ball to material was 6:1. The powder compact was prepared by adding Fe45 powder and the mixed powder into the mold sequentially and was molded using a tablet press (C0514–PP-60S, Tianjin Science and Technology Products, China). Then, the powder compact was vacuum sintered using a carbon tube sintering furnace (ZT-50-22Y, Shanghai Chenhuan Science Technology Corp. Ltd., China) and the sintering temperature was 1,180°C. The scheme of VCp-ZTAp/Fe45 composite material preparation process is shown in Figure 2. The crystal properties of VCp-ZTAp/Fe45 composites were analyzed by Cu Kα radiation using an X-ray diffractometer (XRD, D2 PHASER, Bruker corporation, USA). The operating voltage was 40 kV, the scanning speed was 0.02°/s, and the scanning range was 20–90°. The microstructure of the VCp-ZTAp/Fe45 composites was observed using a scanning electron microscope (SEM, S3400N, Hitachi, Japan). The images provided in the article are secondary electron images.

2.2 Three-body abrasive wear test

Hardox450, 30SiMn and NM450 steels were selected as the control samples. The three-body abrasive wear tests were conducted using a rubber grinding wheel abrasive wear tester (MLG-130, Zhangjiakou Chengxin Testing Equipment Manufacturing Co., Ltd., China). The experiment followed the ASTM-G65 dry sand rubber wheel abrasive wear test standard [27]. Quartz sands with a particle size of 40–70 mesh were used as abrasive, and the sand flow rate was ca. 340 g/min. The diameter of the rubber wheel was 178 mm, and the rotation speed was 200 rpm. The load was 130 N, and the total experimental time was 10 min. Each experiment was repeated at least five times to avoid the influence of other disturbing factors.

After the three-body abrasive wear experiment, the samples were ultrasonic cleaned in ethanol and dried in vacuum. The wear rate was evaluated by the volume loss, which was weighted using an electronic balance (FA2004B, Sahanghai Yueping Instrument Co., Ltd, China) before and after the wear test. The surface topography of the samples and the wear test were observed by SEM.

2.3 Fe45/35SiMnCrMoNi composite casting

During the composite casting, Fe45, instead of VCp-ZTAp/Fe45, was used as the preform (core) to simplify

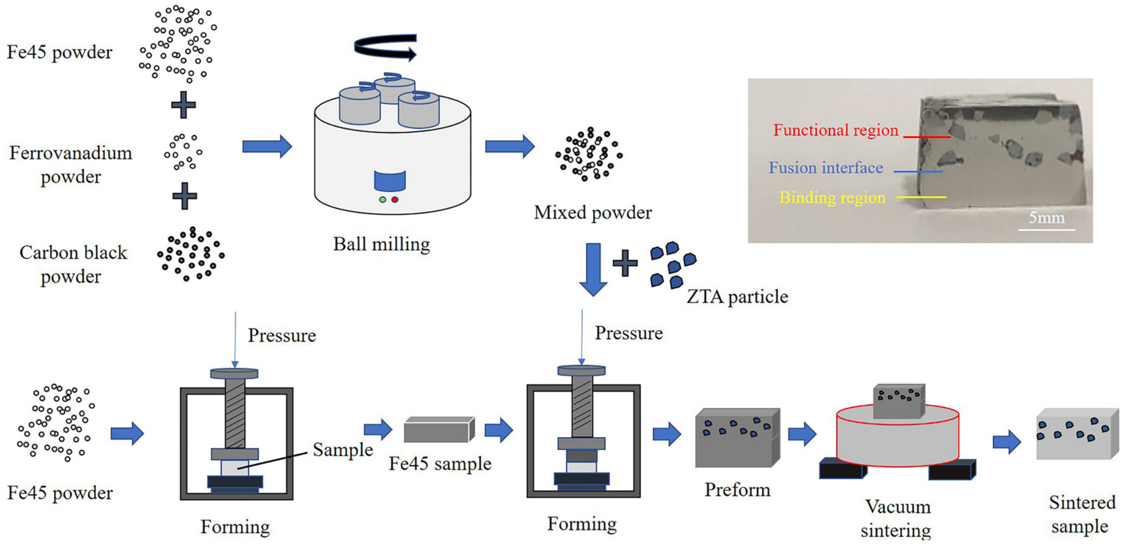

Figure 2: Preparation processes of the VCp-ZTAp/Fe45 composites.

the composite casting process, and the casting molten steel was 35SiMnCrMoNi (element content shown in Table 1). The size of the preform was 40 mm × 13 mm × 13 mm, and the size of the casting was 100 mm × 67 mm × 40 mm. Sand molds were made of industrial water glass sand. The pouring temperature was 1,650°C. After composite casting, the samples were cut, ground, polished and corroded to expose the interface between the preform and the cladding layer. The bonding condition of the interface between preform and cladding was observed using SEM, and the built-in energy dispersive analyzer was used to study the elemental distribution.

The composite casting process was also simulated using the finite element analysis software (ProCAST), including the whole process of filling and solidification. The entire process of filling and curing follows the following assumptions [28].

(1) The incoming liquid metal is evenly distributed only on the inlet of the centrifugal flow part to simulate the smooth filling process of the channel flow part.
(2) The liquid metal is an incompressible Newton fluid.
(3) The inlet is on the inside surface, with one component of inlet velocity parallel to the rotation axis and the other component vertical to the rotation axis.

The continuity and Navier–Stokes equations employed for the filling process of the two parts are as follows:

Continuity equation [29]:

$$D = \frac{\partial u}{\partial x} + \frac{\partial v}{\partial y} + \frac{\partial w}{\partial z}. \tag{1}$$

Navier-Stokes equation [30]:

$$\frac{\partial(\rho\phi)}{\partial t} + \nabla\cdot(\rho\underline{\vec{V}}\phi) = \nabla\cdot(\mu\nabla\underline{\phi}) + S_{\mathrm{u}} - \nabla P, \tag{2}$$

where ρ is the density, ϕ is the velocity component, t is the time, $\underline{\vec{V}}$ is the velocity vector, μ is the dynamic viscosity, S_{u} is the source of the momentum, and p is the pressure. For heat transfer behavior during steel solidification, the following equations are employed [31].

$$\rho c\frac{\mathrm{d}T}{\mathrm{d}t} = \nabla\cdot(k\nabla T) + \dot{Q}, \tag{3}$$

where c is the specific heat, T is the temperature, k is the thermal conductivity, and $\dot{Q}$ is an internal power source.

The critical simulation parameters were set as follows: the initial temperature of the model was 25°C, the pouring temperature was 1,650°C, and the pouring time was 20 s. The preform and the cladding layer formed a metal–metal interface, and the heat transfer coefficient was set to 3,000 W/(m^2 K). The core material and the sand mold formed a metal–sand interface, and the heat transfer coefficient was set 500 W/(m^2 K). The model used the mesh with a 2 mm tetrahedron. The heat dissipation method of the external end-face of the sand mold shell and the end-face of the riser was air cooling, which was set to air cooling (FilmCo = 10, T = 20°C).

3 Results and discussions

This article provides an in-depth analysis of the phase and microstructure of VCp-ZTAp/Fe45 composites. Results show the presence of α-(Fe–Cr–Ni), (Fe, Cr)2B, (Fe, Cr)7C3, Al_2O_3, ZrO_2 and VC in the VCp-ZTAp/Fe45 composite. Among them, α-(Fe–Cr–Ni), (Fe, Cr)2B and (Fe, Cr)7C3 are the main phases of Fe45. Al_2O_3 and ZrO_2 are the main constituent phases of ZTAp. The comparison of the wear performance of VCp-ZTAp/Fe45 composites and Hardox450, 30SiMn and NM450 steels is also shown in this article.

3.1 Phase and microstructure of VCp-ZTAp/Fe45 composites

The following chemical reactions (equations (4)–(9)) may occur during the vacuum sintering of VCp-ZTAp/Fe45, and the standard Gibbs free energy for each reaction could also be calculated [32]. Figure 3 shows the calculated standard Gibbs free energies of Cr_7C_3, V_2C, VC and

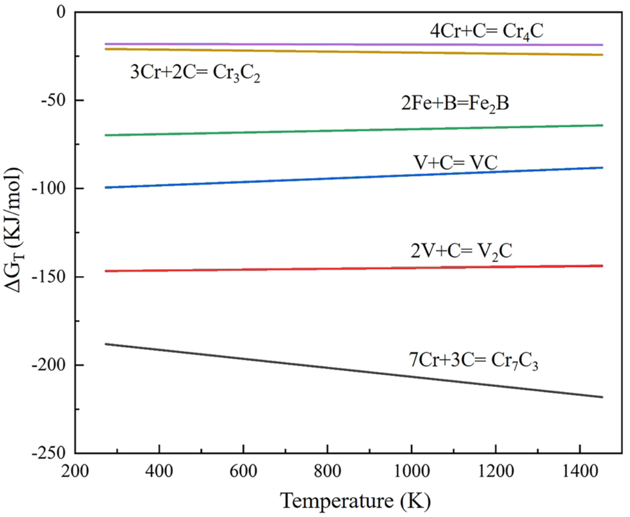

Figure 3: Thermodynamic calculation results of the standard Gibbs free energy.

Fe_2B in the temperature range of 273 K < T < 1,458 K. It is obvious all the calculated results are negative, indicating all the earlier chemical reactions may occur spontaneously during the vacuum sintering process.

$$7Cr + 3C = Cr_7C_3; \quad \Delta G_T = -181.167 - 0.025465T, \tag{4}$$

$$2V + C = V2C; \quad \Delta G_T = -147.277 + 0.002362T, \tag{5}$$

$$V + C = VC; \quad \Delta G_T = -102.100 + 0.00958T, \tag{6}$$

$$2Fe + B = Fe2B; \quad \Delta G_T = -71.128 + 0.004749T, \tag{7}$$

$$4Cr + C = Cr_4C; \quad \Delta G_T = -17.870 - 0.0005T, \tag{8}$$

$$3Cr + 2C = Cr_3C_2; \quad \Delta G_T = -20.07 - 0.00285T. \tag{9}$$

Figure 4 presents the XRD results of the VCp-ZTAp/Fe45 composites. Results show the presence of α-(Fe–Cr–Ni), (Fe, Cr)$_2$B, (Fe, Cr)$_7$C$_3$, Al_2O_3, ZrO_2 and VC in the VCp-ZTAp/Fe45 composite. Among them, α-(Fe–Cr–Ni), (Fe, Cr)$_2$B and (Fe, Cr)$_7$C$_3$ are the main phases of Fe45. Al_2O_3 and ZrO_2 are the main constituent phases of ZTAp. Combined with the thermodynamic calculation results, it can be seen that during the vacuum sintering process, the C element in the raw material reacts with the V element to form a new VC phase. No V_2C could be observed in the material because V_2C has more carbon vacancies, and V_2C is unstable and forms the more stable VC when carbon atoms are sufficient in our experiments. Cr_3C_2 and Cr_4C traces could not be detected in XRD results as well, and this might be due to the small absolute value of ΔG in equations (5) and (6), which means the formation tendency of Cr_3C_2 and Cr_4C is less within the calculated temperature range.

The interface of the ZTAp and the Fe45 matrix in the VCp-ZTAp/Fe45 composites was observed using SEM, as shown in Figure 5. ZTAp well combines with the matrix material and forms a clear and uniform interface. The thermal expansion coefficient of Fe (ca. 10.8 × 10^{-6}/°C) [33] is larger than that of ZTAp (ca. 7.8 × 10^{-6}/°C) [34]. During the sintering cooling process, ZTAp is under compressive stress, while the Fe45 matrix is under tensile stress, which forms thermal expansion dislocation strengthening. In this way, ZTAp and the Fe45 matrix form a solid bonding. The VCp uniformly distributes around the grain boundaries of the Fe45 matrix, as indicated in the yellow square areas in Figure 5. The measured element constitution is V, C, Fe and Cr. The shape of VCp is spherical [23], which could be seen in the Insert in Figure 5.

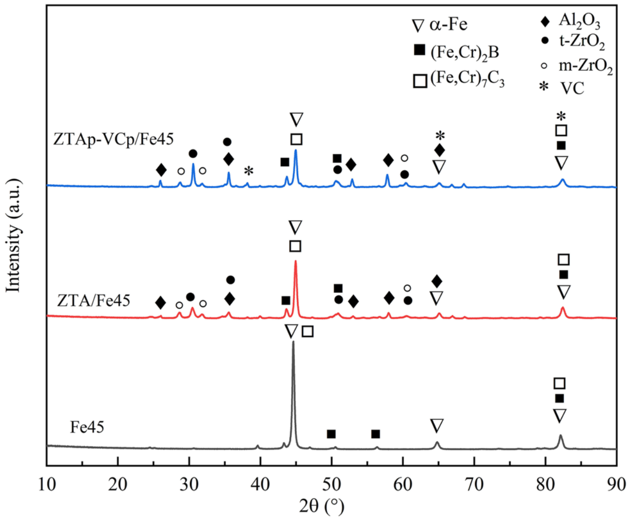

Figure 4: X-Ray diffraction (XRD) results of the VCp-ZTAp/Fe45 composite.

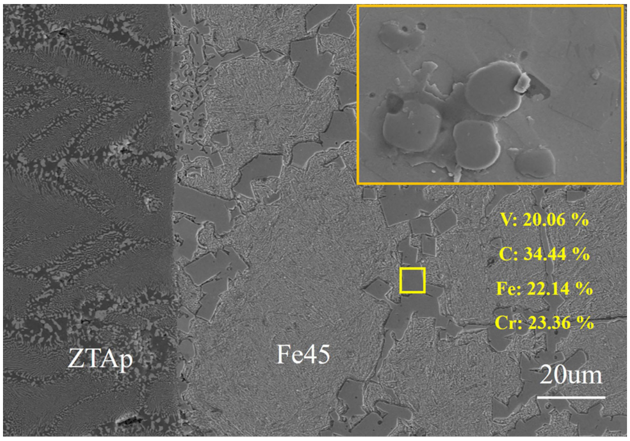

Figure 5: Microstructure of VCp-ZTAp/Fe45 composite by scanning electron microscopy (SEM).

3.2 Anti-wear property of VCp-ZTAp/Fe45 composites

The volume loss of VCp-ZTAp/Fe45 composites and Hardox450, 30SiMn, NM450 steels was measured after the three-body abrasive wear tests; the result of which is shown in Figure 6. Results show that Fe45 alone shows improved anti-wear performance compared with Hardox450, 30SiMn and NM450 steels. The volume loss of the VCp-ZTAp/Fe45 composites is ca. 1/7 that of Hardox450 and NM450, and ca. 1/8 that of 30SiMn, indicating that the anti-wear property of VCp-ZTAp/Fe45 composites is obviously higher than the conventional steel materials.

The wear morphologies of Hardox450, 30SiMn, NM450 steels and VCp-ZTAp/Fe45 composites were observed using SEM, as shown in Figure 7. The wear morphologies of Hardox450, 30SiMn and NM450 steels are very similar, and there are a lot of furrows and pits on their surfaces.

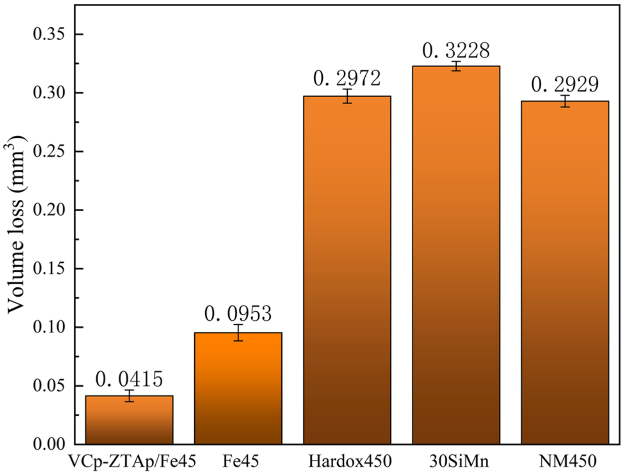

Figure 6: The volume loss measured in the three-body abrasive wear tests.

Comparatively, the number of furrows and pits on the surface of Fe45 is less, which is in line with the volume loss results in Figure 6. Figure 7(e) shows the surface morphology of the VCp-ZTAp/Fe45 composite, and an obvious height difference could be observed between the ZTAp and the Fe45 matrix. Based on the good anti-wear property of Fe45, it could be seen that the ZTAp does not detach from Fe45 after the wear tests, indicating that the bonding between the ZTAp and Fe45 is quite solid. The enlarged image of the ZTAp (area in indicated in the red square in Figure 7e) is shown in Figure 7(f). There are a lot of scratches on the surface of the ZTAp particles because of their protrusion above the matrix, and scratches could be observed on it. Some debris could also be observed around the ZTAp due to its rupture during abrasion. However, only a few furrows and pits could be observed on the surface of the Fe45 matrix, due to its good anti-wear property.

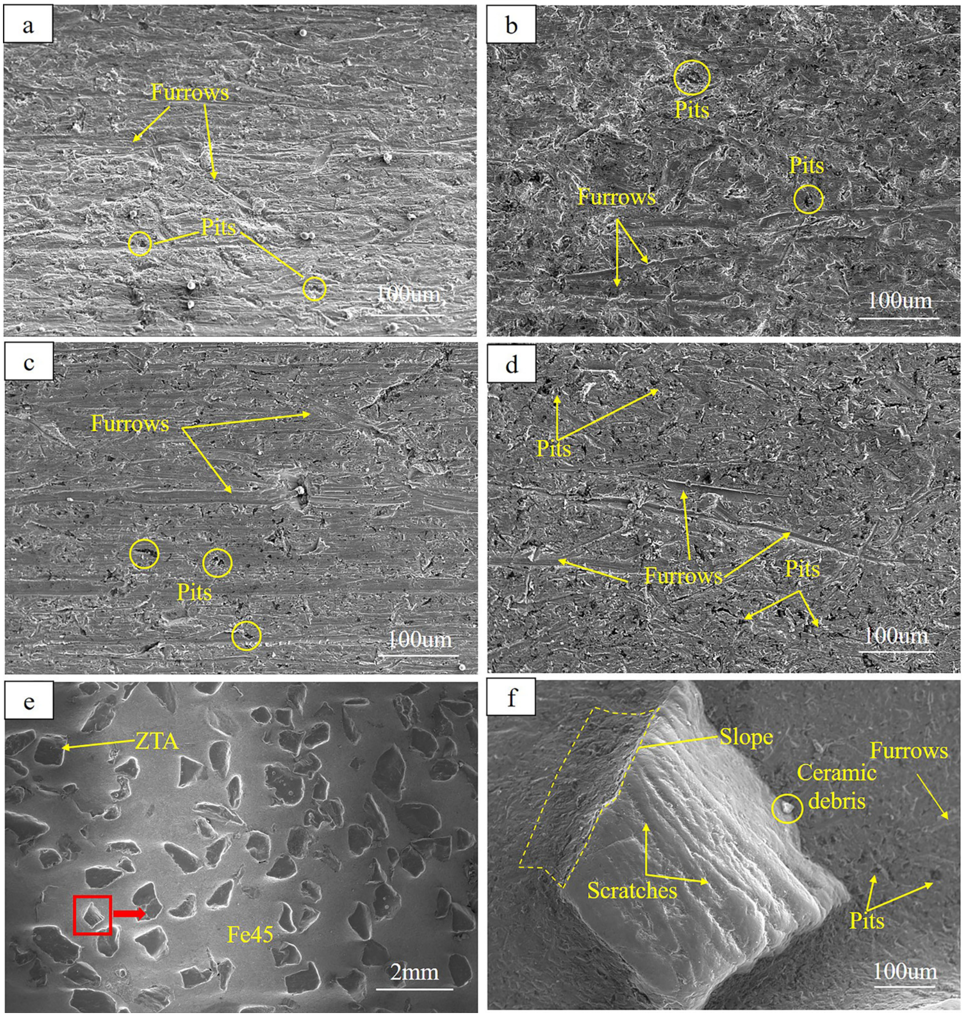

Figure 7: Surface morphology observed using SEM after the three-body abrasive wear tests of (a) Hardox450; (b) 30SiMn; (c) NM450; (d) Fe45; (e) VCp-ZTAp/Fe45 and (f) ZTAp.

Combining the results in Figures 5 and 6, the further enhanced anti-wear performance of VCp-ZTAp/Fe45 composite may be partly due to the existence of VCp. For three-body abrasive wear, the wear volume is positively correlated with the reciprocal ($1/H$) of the material hardness, as is indicated in equation (10) [35]. V is the wear volume, W is the normal force, α is the angle of attack, $\overline{\tan\alpha}$ is the average of $\tan\alpha$, and H is the material hardness. The VCp plays a role in dispersion strengthening [36] and improves the hardness of the matrix. Therefore, there are fewer traces of furrows and pits in the matrix of the VCp-ZTAp/Fe45 composite, and its anti-wear property is thereby improved.

$$V = \frac{2W\overline{\tan\alpha}}{\pi H}. \qquad (10)$$

Figure 8 shows the three-body abrasive wear mechanism of VCp-ZTAp/Fe45 composites. At the initial stage of wear, the abrasives micro-plough the VCp-ZTAp/Fe45 composites under the combined action of tangential stress and normal stress, as shown in Figure 8(b). The matrix area of the VCp-ZTAp/Fe45 composite material all suffers from violent wear, and ZTAp suffers from comparatively gentle wear because the hardness of ZTAp is much higher than that of the Fe45 matrix [17]. ZTAp will gradually protrude from the matrix and form a certain slope with the matrix (as shown in Figure 7f). Therefore, the ZTAp shares large parts of the abrasive force and protects the substrate, reducing the micro-ploughing on the substrate, as shown in Figure 8(c). With the abrasion time prolonged, cracks of ZTAp also appear at the interface between the Al_2O_3 and ZrO_2 phases, forming some debris, as shown in Figure 8(d).

3.3 Fe45/35SiMnCrMoNi bonding property during composite casting

In order to investigate the compatibility between the VCp-ZTAp/Fe45 composite material and the 35SiMnCrMoNi (common material for coal mining equipment) during the composite casting, Fe45 was selected as the core and 35SiMnCrMoNi was selected as the cladding layer. The material thermophysical parameters such as thermal conductivity, specific heat, density, latent heat, and enthalpy

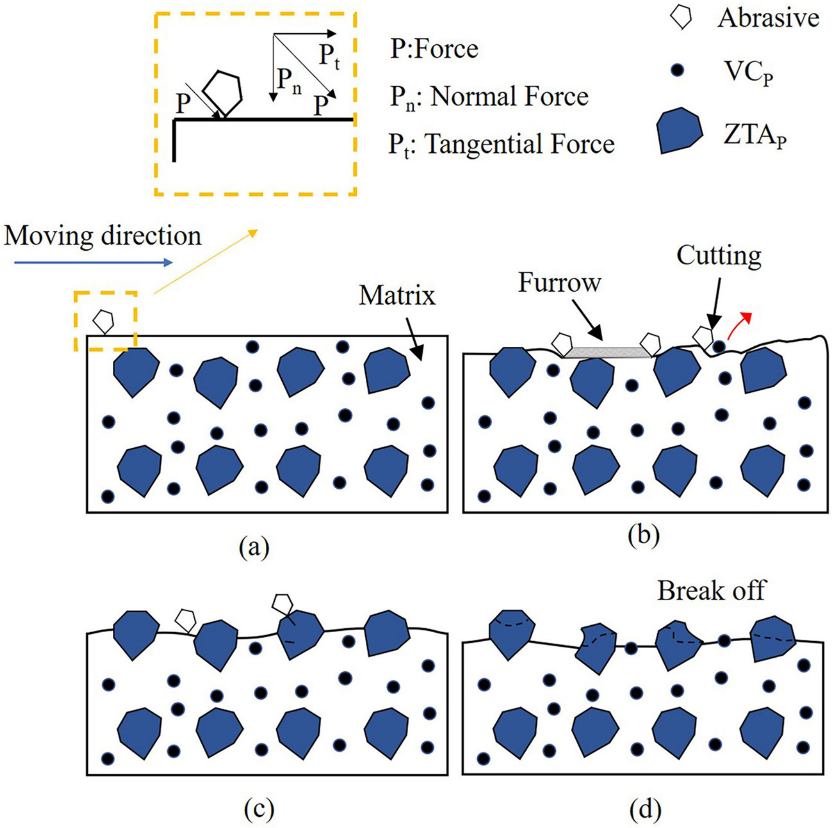

Figure 8: Three-body abrasive wear mechanism of VCp-ZTAp/Fe45. (a) Initial surface; (b) early wear stage; (c) middle wear stage; (d) final wear stage.

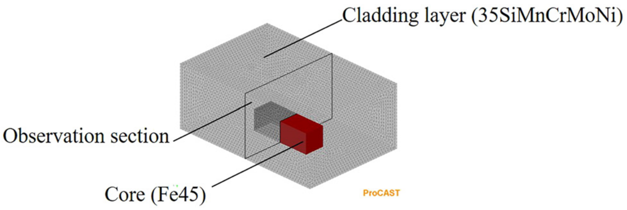

Figure 9: The assembly of the core (Fe45) and the cladding layer (35SiMnCrMoNi).

may change with the temperature [37–40]. During the casting process, the thermophysical parameters directly affect the heat transfer and temperature changes, and therefore, they need to be calculated before the temperature field calculation. Since the material involves the release of the latent heat of solidification during the phase transition process, the fraction solid, the solidus and liquidus of the material are also important for simulation calculations. By using ProCAST software, the solidus of Fe45 is calculated 1,202°C, and the liquidus of Fe45 is 1,350°C. The solidus of 35SiMnCrMoNi calculated is 1,131°C and the liquidus of 35SiMnCrMoNi is 1,490°C. The thermal conductivity of Fe45 and 35SiMnCrMoNi increases gradually with the increased temperature. When the phase transition occurs, the enthalpy suddenly changes. The enthalpy of Fe45 changes abruptly at 1,200–1,350°C, and the enthalpy of 35SiMnCrMoNi changes abruptly at 1,200–1,500°C, which corresponds to the release of the latent heat of fusion of Fe45 and 35SiMnCrMoNi during the phase transformation process. The change in material density is the main cause of material solidification shrinkage. With the decreased temperature, the molecular motion of the material is less active, and the density increases. The density of Fe45 and 35SiMnCrMoNi decreases abruptly between 1,200–1,350 and 1,200–1,500°C, respectively due to the solidification process of the materials.

The assembly of the core (Fe45) and cladding layer (35SiMnCrMoNi) is shown in Figure 9, a cross-sectional view of which is also shown in this figure to make it clear to the readers. The temperature field and fraction solid distribution of the Fe45/35SiMnCrMoNi interface are shown in Figure 10. The temperature of the Fe45 is obviously affected by the high temperature of molten 35SiMnCrMoNi during the casting process. The temperature of the upper surface and upper corners of the Fe45 shows the most obvious increase, and the high-temperature area gradually spread from the top to the center and the bottom of Fe45. At 6 s, the molten metal completely wraps the Fe45. At 12 s, the temperature of the upper area of Fe45 reaches the solidus temperature. At the same time, the fraction solid of the Fe45 decreases, and the upper area is at a solid–liquid coexistence state. At 16 s, sand mold filling is complete, and the top of Fe45 reaches the liquidus temperature. At 50 s, the whole Fe45 core reaches the liquidus temperature, and the molten 35SiMnCrMoNi steel is at liquid or solid–liquid coexistence state. Due to the good diffusion properties of the liquid phase, atoms at the interface of Fe45 and 35SiMnCrMoNi could easily exchange to form a metallurgical bond at this moment.

The interface after casting was observed by SEM, as shown in Figure 11(a). The structure of the cladding layer (35SiMnCrMoNi) is tempered sorbite, and the Fe45 matrix of the VCp-ZTAp/Fe45 composite material is mainly ferrite. Fe45 and 35SiMnCrMoNi are well combined, forming a clear and tight interface with a thickness of ca. 80 um. Neither pores nor other defects could be observed,

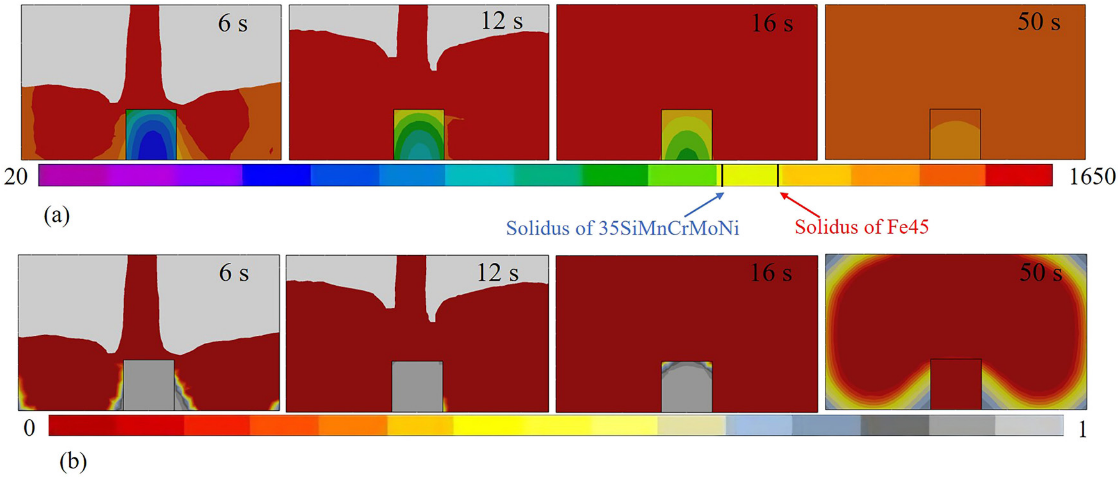

Figure 10: (a) Temperature and (b) fraction solid of core (Fe45) and cladding layer (35SiMnCrMoNi).

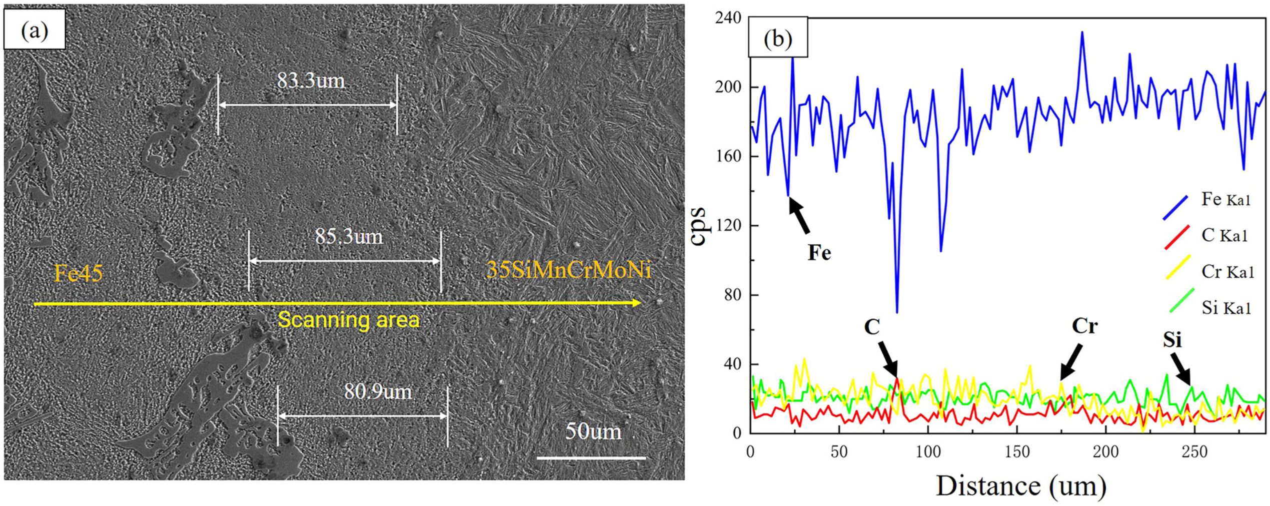

Figure 11: Interface morphology of Fe45/35SiMnCrMoNi after composite casting. (a) SEM image of the interface; (b) EDS results of the interface.

indicating the bonding formed is solid. The elemental distribution along the bonding interface is shown in Figure 11(b). Elements such as Fe, C and Si evenly distribute along the bonding area. The content of Cr gradually decreases from the left part (Fe45) to the right part (35SiMnCrMoNi), indicating that the bonding formed between the two materials is the metallurgical bond. In a word, all the above results prove that in the process of pouring and solidification of 35SiMnCrMoNi molten steel on Fe45 matrix within 50 s, the elements completely interdiffuse at the interface, forming a robust interfacial bonding. The results show that the substrate of the VCp-ZTAp/Fe45 composite material has good compatibility with the 35SiMnCrMoNis steel during the composite casting process.

4 Conclusions

In order to improve the anti-wear performance of key components of mining equipment and its service life, gradient-distributed vanadium carbide-zirconia toughened alumina particles reinforced iron matrix (VCp-ZTAp/Fe45) composites were prepared by vacuum sintering in order to obtain the good anti-wear performance. Three-body abrasive wear experiments were carried out to investigate its anti-wear performance. Besides, the composite casting process of Fe45 (core) and 35SiMnCrMoNi (cladding material) was investigated by using the FEM, and the bonding property was studied.

Results show that the VCp-ZTAp/Fe45 composite material has excellent anti-wear properties than the mining wear-resistant steel currently used. The wear volume of VCp-ZTAp/Fe45 composite is ca. 1/7 of Hardox450 and NM450 and ca. 1/8 of 30SiMn. The spherical VC particle disperses along the grain boundaries of Fe45 and forms the dispersion strengthening of the matrix, thus improving its mechanical strength. The three-body abrasive wear mechanism of VCp-ZTAp/Fe45 composites was also revealed. The results from the FEM calculation of the casting process of Fe45/35SiMnCrMoNi indicate that both materials can be in liquid or solid–liquid coexistence state at the same time during the casting process within 50 s. At this time, the elements of Fe45 and 35SiMnCrMoNi can interdiffuse well at the interface of the Fe45/35SiMnCrMoNi to form a robust metallurgical bonding, with a ca. 80 um thickness of the bonding area. All these results prove the as prepared VCp-ZTAp/Fe45 composite material is quite promising in the application as the anti-wear material for mining equipment and has good compatibility with other steel during the composite casting process.

Acknowledgements: The work was supported by the State Key Laboratory of Tribology in Advanced Equipment (No. SKLTKF20B11 and SKLTKF21A01), Fundamental Research Funds for the Central Universities (No. 2021YQJD21 and 2021XJJD01), and Natural Science Foundation of Beijing Municipality (No.22C10149). The authors thank Dr. Yang Qin from China University of Mining and Technology-Beijing for the constructive suggestions in three-body abrasive wear tests.

Conflict of interest: Authors state no conflict of interest.

References

[1] Chupin S, Bolobov V. Influence of thermomechanical treatment modes on wear resistance of mining equipment material.

Mater Sci Forum. 2019;945:695–9. doi: 10.4028/www.scientific.net/MSF.945.695.

[2] Shi Z, Zhu Z. Case study: Wear analysis of the middle plate of a heavy-load scraper conveyor chute under a range of operating conditions. Wear. 2017;380–381:36–41. doi: 10.1016/j.wear.2017.03.005.

[3] Chen W, Biswas S, Roberts A, O'Shea J, Williams K. Abrasion wear resistance of wall lining materials in bins and chutes during iron ore mining. Int J Miner Process. 2017;167:42–8. doi: 10.1016/j.minpro.2017.08.002.

[4] Holmberg K, Kivikytö-Reponen P, Härkisaari P, Valtonen K, Erdemir A. Global energy consumption due to friction and wear in the mining industry. Tribol Int. 2017;115:116–39. doi: 10.1016/j.triboint.2017.05.010.

[5] Feldshtein EE, Dyachkova LN. Wear minimization for highly loaded iron-based MMCs due to the formation of spongy-capillary texture on the friction surface. Wear. 2020;444–5. doi: 10.1016/j.wear.2019.203161.

[6] Bai H, Zhong L, Cui P, Shang Z, Lv Z, Xu Y. Microstructure and compressive properties of V–V8C7/Fe core-shell rod-reinforced iron-based composite fabricated via two-step *in-situ* reaction. Vacuum. 2020;176:109302. doi: 10.1016/j.vacuum.2020.109302.

[7] Ru J, He H, Jiang Y, Zhou R, Hua Y. Ionic liquid-assisted preparation of Ni–Cr dual wrapped ZTA particles for reinforced iron-based composites. Adv Eng Mater. 2019;21(5):1801120. doi: 10.1002/adem.201801120.

[8] Dyachkova LN, Feldshtein EE, Vityaz PA, Mikhalski M. Tribological properties of iron-based powder composite materials with addition of graphite, alumina and zirconia nanoparticles. J Frict Wear. 2020;41(3):198–203. doi: 10.3103/s1068366620030046.

[9] Ma M, Sun W-C, Zhang Y-G, Liu X-J, Dong Y-R, Zi J-Y, et al. Effect of TiC particles concentration on microstructure and properties of Ni-TiC composite coatings. Mater Res. 2019;22(6):e20190530. doi: 10.1590/1980-5373-mr-2019-0530.

[10] AlMangour B, Grzesiak D, Yang J-M. *In situ* formation of TiC-particle-reinforced stainless steel matrix nanocomposites during ball milling: Feedstock powder preparation for selective laser melting at various energy densities. Powder Technol. 2018;326:467–78. doi: 10.1016/j.powtec.2017.11.064.

[11] Sharma BP, Rao GS, Vates UK. Powder metallurgy processing and mechanical characterization of iron-based composite reinforced with alumina and zirconium diboride. In Advances in Industrial and Production Engineering. Lecture Notes in Mechanical Engineering; 2019. p. 303–8. doi: 10.1007/978-981-13-6412-9_28.

[12] Shen P, Zhang L, Fu J, Zhou H, Wang Y, Cheng L. The effect of Al content on the wettability between liquid iron and MgO Al2O3 binary substrate. Ceram Int. 2019;45(9):11287–95. doi: 10.1016/j.ceramint.2019.02.205.

[13] Yang J, Cai X, Fu Y, Xu Y, Li X. Evaluation of growth behaviour of vanadium carbides-reinforced iron-based surface compound layer by *in-situ* reaction. Vacuum. 2019;166:178–83. doi: 10.1016/j.vacuum.2019.04.057.

[14] Jin X, Li Y, Chen B, Fan H, Feng K, Cui H. Microstructure and tribological properties of WC reinforced iron-based hard-facing alloy. IOP Conference Series: Materials Science and Engineering. Vol. 493, 2019. p. 012093. doi: 10.1088/1757-899x/493/1/012093.

[15] Li C, Li Y, Wang J, Li B, Yi D, Shi J, et al. Microstructure and mechanical properties of Fe matrix composites reinforced by nickel–chromium double-layer coated ZTAP ceramics. Ceram Int. 2020;46(10):16993–7002. doi: 10.1016/j.ceramint.2020.03.284.

[16] Zhou M, Jiang Y, Sui Y. Microstructure and properties of interfacial transition zone in ZTA particle–reinforced iron composites. Appl Phys A. 2019;125(2):1–10. doi: 10.1007/s00339-018-2365-z.

[17] Wang Y, Qin Y, Fu D, Chen H, Pan Y, Zhu C, et al. Behaviors of ZTA (zirconia toughened alumina) reinforced iron composites under impact abrasive wear conditions. Wear. 2020;458–9. doi: 10.1016/j.wear.2020.203397.

[18] Li P, Gao J, Gong M, Shen D, Tong W. Effects of manganese on diffusion and wear behavior of ZTA particles reinforced iron matrix composites in vacuum. Vacuum. 2020;177:109408. doi: 10.1016/j.vacuum.2020.109408.

[19] Fan L, Wang Q, Yang P, Chen H, Hong H, Zhang W, et al. Preparation of nickel coating on ZTA particles by electroless plating. Ceram Int. 2018;44(10):11013–21. doi: 10.1016/j.ceramint.2018.03.055.

[20] Aouni A, Weisbecker P, Loi TH, Bauer-Grosse E. Search for new materials in sputtered V1–xCx films. Thin Solid Films. 2004;469–470:315–21. doi: 10.1016/j.tsf.2004.08.139.

[21] Feng K, Hong M, Yang Y, Wang W. Combustion synthesis of VC/Fe composites under the action of an electric field. Int J Refract Met Hard Mater. 2009;27(5):852–7. doi: 10.1016/j.ijrmhm.2009.04.001.

[22] Wang RF, Sun ZP, Zhang GJ, Zou LY. Effect of VC content on microstructure and mechanical properties of VC/Fe-based composites. Adv Mater Res. 2012;583:219–22. doi: 10.4028/www.scientific.net/AMR.583.219.

[23] Wang J, Fu S. Production of *in situ* vanadium carbide particulate reinforced iron matrix composite. Mater Sci. 2014;20(4):409–13. doi: 10.5755/j01.ms.20.4.6445.

[24] Tayal RK, Kumar S, Singh V, Gupta A, Ujjawal D. Experimental investigation and evaluation of joint strength of A356/Mg bimetallic fabricated using compound casting process. Int J Metalcasting. 2018;13(3):686–99. doi: 10.1007/s40962-018-0288-2.

[25] Bakke AO, Arnberg L, Li Y. Achieving high-strength metallurgical bonding between A356 aluminum and copper through compound casting. Mater Sci Eng: A. 2021;810:140979. doi: 10.1016/j.msea.2021.140979.

[26] Fan S, Wu H. Improved interface bonding of Mg/aluminized steel bimetallic castings prepared by solid–liquid compound casting process. Int J Cast Met Res. 2020;34(1):32–42. doi: 10.1080/13640461.2020.1868147.

[27] Doering A, Danks D, Mahmoud S, Scott J. Evaluation of ASTM G65 abrasive – Spanning 13 years of sand. Wear. 2011;271(9–10):1252–7. doi: 10.1016/j.wear.2011.01.051.

[28] Lu S-L, Xiao F-R, Zhang S-J, Mao Y-W, Liao B. Simulation study on the centrifugal casting wet-type cylinder liner based on ProCAST. Appl Therm Eng. 2014;73:512–21. doi: 10.1016/j.applthermaleng.2014.07.073.

[29] McBride D, Humphreys N, Croft T, Green N, Cross M, Withey P. Complex free surface flows in centrifugal casting: Computational modelling and validation experiments. Comput Fluids. 2013;82:63–72. doi: 10.1016/j.compfluid.2013.04.021.

[30] Wang J, Fu P, Liu H, Li D, Li Y. Shrinkage porosity criteria and optimized design of a 100-ton 30Cr2Ni4MoV forging ingot.

Mater & Des. 2012;35:446–56. doi: 10.1016/j.matdes.2011.09.056.

[31] Lan P, Zhang J. Study on the mechanical behaviors of grey iron mould by simulation and experiment. Mater & Des. 2014;53:822–9. doi: 10.1016/j.matdes.2013.07.077.

[32] Arasteh J, Akbari GH. Microstructural evolution during high-energy mechanical alloying of immiscible Zr–Cr alloy. J Mater Res. 2020;35(14):1825–36. doi: 10.1557/jmr.2020.160.

[33] Sahraeinejad S, Izadi H, Haghshenas M, Gerlich AP. Fabrication of metal matrix composites by friction stir processing with different particles and processing parameters. Mater Sci Eng: A. 2015;626:505–13. doi: 10.1016/j.msea.2014.12.077.

[34] Kumar R, Madhu S, Aravindh K, Jayakumar V, Bharathiraja G, Muniappan A. Casting design and simulation of gating system in rotary adaptor using procast software for defect minimization. Mater Today: Proc. 2020;22:799–805. doi: 10.1016/j.matpr.2019.10.156.

[35] Zheng B, Li W, Tu X, Song S, Huang W. Effect of ZTA ceramic particles strengthened high chromium white cast iron on three-body abrasion behavior. Mater Res Express. 2019;6(11):116581. doi: 10.1088/2053-1591/ab489c.

[36] Qin YQ, Tian Y, Peng YQ, Luo LM, Zan X, Xu Q, et al. Research status and development trend of preparation technology of ceramic particle dispersion strengthened copper-matrix composites. J Alloy Compd. 2020;848:156475. doi: 10.1016/j.jallcom.2020.156475.

[37] Guo J, Li Y, Fu J. Design and improvement of the investment casting process for the ring-shaped Aluminum alloy based on PROCAST software. IOP Conference Series: Materials Science and Engineering. Vol. 382, 2018. p. 042006. doi: 10.1088/1757-899x/382/4/042006.

[38] Fu Y, Wang H, Zhang C, Hao H. Numerical simulation and experimental investigation of a thin-wall magnesium alloy casting based on a rapid prototyping core making method. Int J Cast Met Res. 2017;31(1):37–46. doi: 10.1080/13640461.2017.1365477.

[39] Liu JG, Yang L, Fang XG, Li B, Yang YW, Fang LZ, et al. Numerical simulation and optimization of shell mould casting process for leaf spring bracket. China Foundry. 2020;17(1):35–41. doi: 10.1007/s41230-020-9089-3.

[40] Javahery M, Abbasi M. Simulation of casting process: case study on the gating and feeding design for outlet diaphragms of iron ore ball mill. Heat Mass Transf. 2018;55(7):1959–67. doi: 10.1007/s00231-018-2447-7.